ACS Photonics
Article
pubs.acs.org/journal/apchd5

Sharply Focused Azimuthally Polarized Beams with Magnetic Dominance: Near-Field Characterization at Nanoscale by Photoinduced Force Microscopy

Jinwei Zeng, Fei Huang, Caner Guclu, Mehdi Veysi, Mohammad Albooyeh, H. Kumar Wickramasinghe,* and Filippo Capolino*

Department of Electrical Engineering and Computer Science, University of California Irvine, Irvine, California 92697, United States

Supporting Information

ABSTRACT: Azimuthally polarized beams are gaining fundamental importance for near-field force microscopy systems to inspect photoinduced magnetism in special molecules or nanostructures, due to their strong axial magnetic field and vanishing electric field. The magnetic dominant region represents a unique trait of such a beam as a potentially ideal structured light to probe photoinduced magnetism at the nanoscale. Therefore, we present a near-field characterization of an optical, sharply focused azimuthally polarized beam using photoinduced force microscopy, a technique with simultaneous near-field excitation and detection, achieving nanoscale resolution well beyond the diffraction limit. Such a method exploits the photoinduced gradient force on a nanotip, mechanically detected as forced oscillations of the cantilever in an atomic force microscopy system upon external light illumination. The photoinduced force is strongly localized, which that depends only on the near-field signal free from background scattering photons, granting photoinduced force microscopy a superior performance over its precedent near-field scanning optical microscopy. We develop an analytical model to correct the tip-induced measurement anisotropy, suppress the background noise, and reveal the local electric field distribution of the azimuthally polarized beam. These measurements are used to retrieve its strong longitudinal axial magnetic field at the center of the polarization vortex where the electric field vanishes. This study can lead to a plethora of possibilities in optomechanical, chemical, or biomedical applications. We also propose and discuss how to use such beams with polarization azimuthal symmetry as a way to calibrate microscope nanotips.

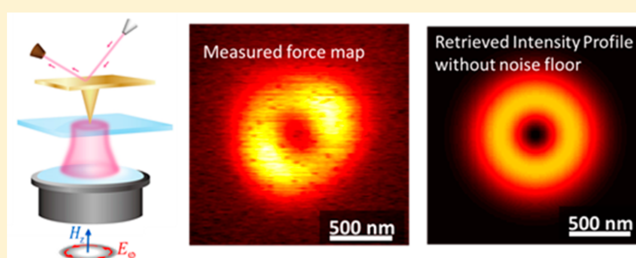

KEYWORDS: *photoinduced force microscopy, azimuthally polarized beam, structured light, magnetic dominance, magnetic probing light*

Counterintuitive yet intriguing and desired, an azimuthally polarized beam (APB) exhibits unusual optical properties that are much needed for state-of-the-art research on photoinduced magnetic force microscopy (PiMFM) and nanoscale manipulation.[1−4] The APB has azimuthal electric field polarization with a null on the beam axis, where the longitudinal magnetic field peaks. Hence, the beam axial region exhibits a magnetic dominance with respect to the electric field, denoted by the figure of merit $F_Y = \eta|\mathbf{H}|/|\mathbf{E}|$, which represents a normalized local field admittance to that of a plane wave as was defined in ref 5, where η is the plane wave impedance and $|\mathbf{E}|$ and $|\mathbf{H}|$ are the electric and magnetic field magnitudes, respectively. In contrast to the free-space normalized field admittance for a plane wave with $F_Y = 1$ or for a fundamental Gaussian beam with $F_Y < 1$ (where F_Y approaches unity as the Gaussian beam waist increases), in the vicinity of the APB axis the normalized admittance yields $F_Y \gg 1$, with $F_Y \to \infty$ when approaching the axis, where a purely longitudinal magnetic field exists.[4,6] Such a longitudinal magnetic field in the axial region can be enhanced by sharp focusing.[2,3] This characteristic of magnetic dominance around the axial region in APBs makes these beams ideal illumination sources for investigating light−matter interaction based on the magnetic component of light interacting with matter magnetic dipole transitions at optical frequency.[7−10] Shielding matter from the electric field is also essential for excluding electric dipole transitions in matter shadowing the elusive photoinduced magnetic transitions. Interrogating these features of APB is a significant step to drive forward the rapid development of optical magnetic field manipulation, microscopy, and sensing applications in life science and nanotechnology.[11,12]

Having the aforementioned applications in mind, the study of sharply focused APBs is challenged by the difficulty of beam characterization owing to its nanoscale features.[4,6,13−15] In many realistic applications of APBs as sensor or microscope sources, sharp focusing of the incident beam is often necessary for field enhancement to achieve a decent sensitivity and

Received: July 23, 2017
Published: October 12, 2017

Downloaded via UNIV OF CALIFORNIA IRVINE on August 28, 2018 at 08:23:09 (UTC).
See https://pubs.acs.org/sharingguidelines for options on how to legitimately share published articles.

© 2017 American Chemical Society

DOI: 10.1021/acsphotonics.7b00816
ACS Photonics 2018, 5, 390−397

resolution.[16] Sharp focusing reduces the beam size close to the wavelength, and its critical features of the donut profile can be even much smaller than a wavelength.[6,17] A finer direct interrogation of the APB features is therefore limited by resolution of conventional photodetectors.

A typical approach in modern optics to investigate the optical field distribution beyond the diffraction limit is using near-field scanning optical microscopy (NSOM).[18−30] By placing the scanning probe very close to a surface under particular illumination, the NSOM is able to interact with the evanescent field scattered from the surface and converts it to propagating waves to be measured by photodetectors in the *far-field region*. Thus, the NSOM can have a high resolution due to the super spatial resolute intensity of the local evanescent field, which in principle is only limited by the size of the probe on the nanoscale.[16,19,21−23] On the other hand, due to the far-field detection, the NSOM intrinsically suffers from a significant noise from the background scattering photons surrounding the probe, which sometimes can even overwhelm the signal.[17,24,25] This noise makes a generally very poor signal-to-noise ratio of NSOM characterization especially in inspecting subwavelength feature of sharply focused structured light.[13,28−30] Although some studies show that the background noise can be suppressed by interferometry-based detection methods,[13,26,27] these methods also make the NSOM microscopy system considerably complicated and delicate, difficult to establish, and maintain stable.

With the goal of reducing the high background scattering noise from the NSOM, a new microscopic technique named photoinduced force microscopy (PiFM) has been recently developed to overcome this deficiency.[17,24,31−35] The PiFM characterizes the optical field distribution by examining the near-field photoinduced electric dipole−dipole interaction force between the sample surface and the probe tip in a modified atomic force microscopy (AFM) system, from which both the excitation and detection of the optical response are in the near field. The photoinduced dipole−dipole interaction force is strongly localized and will decay rapidly while increasing the distance between the tip and the scattering source. Thus, the background noise, which is mainly nonlocal to the probe tip, is efficiently eliminated. Furthermore, the PiFM is comparably simple and convenient to operate since it is typically based on the well-established AFM systems. Here, as shown in Figure 1, we use the PiFM to map the subwavelength field distribution of a sharply focused APB, fit the distribution by analytical modeling, and calculate the APB crucial features in realistic cases, such as the magnetic and the electric field intensity distributions at the focal plane. This work shows, for the first time, such near-field direct interrogation of a sharply focused APB with nanoscale resolution by measuring photoinduced force using the PiFM.

■ APB ANALYTICAL EXPRESSION AND BASIC PHYSICS

The sharply focused APB field at the focal plane is represented by the superposition of two Laguerre Gaussian (LG) beams in their minimum waist based on a paraxial wave expression.[5,8] In particular the paraxial electric field expression for an ideal monochromatic APB in a cylindrical coordinate system is expressed as a superposition of a left- and a right-hand circularly polarized LG beam, carrying orbital angular momentum (OAM) with orders of +1 and −1, respectively,[2,3] as

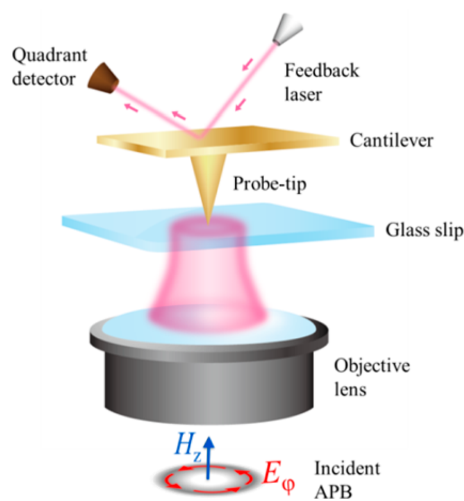

Figure 1. Schematic of a PiFM that measures the subwavelength field intensity distribution of a sharply focused APB. The field intensity is mechanically detected as forced oscillations of the cantilever of an atomic force microscope upon external light excitation of the tip−sample region.

$$\mathbf{E}_\varphi = \frac{-\mathrm{i}\sqrt{2}}{2}(u_{-1,0}\hat{\mathbf{e}}_{\mathrm{RH}} - u_{1,0}\hat{\mathbf{e}}_{\mathrm{LH}})\mathrm{e}^{ikz} = \frac{-\mathrm{i}\sqrt{2}}{2}\frac{u_{\pm1,0}}{\mathrm{e}^{\pm i\varphi}}\mathrm{e}^{ikz}\hat{\mathbf{e}}_\varphi = \frac{-\mathrm{i}\sqrt{2}}{2}E_\varphi\hat{\mathbf{e}}_\varphi \quad (1)$$

Here $\hat{\mathbf{e}}_\varphi$, $\hat{\mathbf{e}}_{\mathrm{RH}}$, and $\hat{\mathbf{e}}_{\mathrm{LH}}$ denote azimuthal, right-handed circular, and left-handed circular polarization unit vectors, respectively; $E_\varphi = u_{\pm1,0}\mathrm{e}^{\mp i\varphi}\mathrm{e}^{ikz}$ is the azimuthal field component, and $u_{\pm1,0}$ is the LG beam under paraxial approximation given by

$$u_{\pm1,0} = \frac{V}{\sqrt{\pi}}\frac{2\rho}{w^2}\mathrm{e}^{-(\rho/w)^2\zeta}\mathrm{e}^{-2\mathrm{i}\tan^{-1}(z/z_{\mathrm{R}})}\mathrm{e}^{\pm i\varphi}$$
$$w = w_0\sqrt{1 + (z/z_{\mathrm{R}})^2},\ \zeta = (1 - \mathrm{i}z/z_{\mathrm{R}}) \quad (2)$$

where V is a magnitude constant, $z_{\mathrm{R}} = \pi w_0^2/\lambda$ is the Rayleigh distance, and $k = 2\pi/\lambda$ and λ are the wavenumber and wavelength in the host medium, respectively. The parameter w_0 is called the *beam parameter*, which controls the transverse spatial extent of the beam at its paraxial minimum-waist plane (i.e., $z = 0$). A comprehensive APB theoretical description is given in refs 2 and 8. An ideal APB's electric field given in eq 1 has an annular-shaped intensity profile that is characterized next at its minimum-waist plane ($z = 0$). The complementary full width at half-maximum (CFWHM) for the APB is defined as the transverse width across the null of its annular-shaped intensity profile in the minimum-waist plane where the electric field intensity is smaller than half of its maximum.[8] The CFWHM and the radial location of the electric field peak of the APB at its minimum-waist plane ($z = 0$) are calculated as[8]

$$\mathrm{CFWHM}(E_\varphi)|_{z=0} \approx 0.68w_0$$
$$\rho_{\mathrm{M}}|_{z=0} = w_0/\sqrt{2} \quad (3)$$

These quantities are important to characterize the APB's electric field and are retrieved next using force measurements.

Optical Setup to Generate the APB. In this work the APB is generated by transmitting a linearly polarized plane wave through a commercial polarization converter from ARCoptix. The principle of the polarization converter to

DOI: 10.1021/acsphotonics.7b00816
ACS Photonics 2018, 5, 390−397

acquire vector polarization is explained in ref 36. The polarizer converter consists of a specially arranged, pixel-based spatially inhomogeneous liquid crystal molecule array, in which each liquid crystal pixel functions as an effective half-wave plate element. Therefore, the total polarization conversion is obtained by a spatial distribution of transmitted fields whose local polarization is rotated compared to the incident beam's polarization. A built-in half-wave retarder is placed on the top half of the converter to correct the phase distribution of the generated vector beam, which will thus exhibit parallel fringes due to the diffraction in the defect line at the boundary of the half-wave retarder. Here the laser beam at approximate 670 nm is first transmitted through a Bragg cell to enable the frequency modulation needed from the PiFM, as shown in Figure 2, then coupled into a single-mode fiber to clean the beam distortion caused by the Bragg cell. The beam is then collimated, polarized, and transmitted through the polarization converter to generate the APB to the PiFM. The power of the final incident beam into the PiFM system is about 90 μW. The schematic of the optical setup and the generated APB and its polarization analysis are shown in Figure 2 before tight focusing. The generated APB in donut shape is shown by the captured charge coupled device (CCD) image. Polarization analysis in Figure 2 is performed by transmitting the generated APB through a linear polarization analyzer, and it is observed that the transmitted beam has a double-lobe profile in which the dark line is always parallel to the rotating analyzer axis, demonstrating an excellent azimuthal polarization.

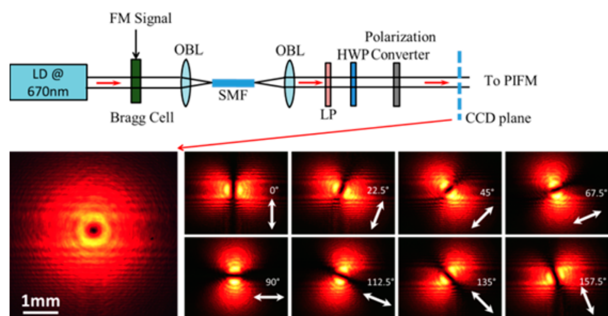

Figure 2. (Top) Schematic of the optical setup to generate APB. OBL: objective lens, SMF: single-mode fiber, LP: linear polarizer, FM: frequency modulation, HWP: half-wave plate. (Bottom) CCD image of the generated APB and the polarization analysis of the transmitting APB through a linear polarization analyzer in which the polarization axis is indicated by the white arrow. This APB will be sharply focused when used as illumination in a PiFM.

■ ORIGIN OF THE PHOTOINDUCED FORCE IN PIFM

The APB is focused by a high-numerical-aperture (NA) oil-immersion objective lens (NA = 1.45) into the PiFM system to characterize its field distribution, as shown in Figure 3. The principle of PiFM has been discussed previously.[17,24,29,33,37,38] We recall that similarly to the standard AFM, the PiFM utilizes a nanoscaled probe tip on a vibrating cantilever to feel the interaction force between the tip and the sample surface, where the amount of the interaction force is indicated by the change of the cantilever's vibration amplitude. Note that the total tip—sample interaction force contains both photoinduced force and nonphotoinduced force, in which the photoinduced force is selectively extracted by a lock-in mechanism, which will be explained in the next section. The illuminating electromagnetic field induces charge and current densities $\rho(\mathbf{r}, t)$ and $\mathbf{J}(\mathbf{r}, t)$ on the cantilever tip. Therefore, the photoinduced force on the tip volume V due to the electromagnetic excitation is determined by the Lorentz force[39] $\mathbf{F}(t) = \int_V[\rho(\mathbf{r}, t)\, \mathbf{E}(\mathbf{r}, t) + \mathbf{J}(\mathbf{r}, t) \times \mathbf{B}(\mathbf{r}, t)]\, dv$, where $\mathbf{E}(\mathbf{r}, t)$ and $\mathbf{B}(\mathbf{r}, t)$ are the total electric field and magnetic induction vectors at the tip. By using the conservation law for the momentum and applying Maxwell's equations for the electromagnetic fields in the Lorentz force formula, the time-averaged optical force is obtained as[39] $\langle \mathbf{F} \rangle_t = \int_V \langle \nabla \cdot \underline{\mathbf{T}}(\mathbf{r}, t) \rangle_t\, dv$ where $\underline{\mathbf{T}} = \varepsilon_0 \mathbf{E}\mathbf{E} + \mu_0 \mathbf{H}\mathbf{H} - 1/2(\varepsilon_0 E^2 + \mu_0 H^2)\underline{\mathbf{I}}$ is the Maxwell stress tensor (underline denotes tensors of second rank). Here $\underline{\mathbf{I}}$ is the identity tensor, $\mathbf{E}$ and $\mathbf{H}$ are the electric and magnetic fields, respectively, and the symbol $\langle \rangle_t$ denotes time average. It can be shown that in the dipole approximation regime, valid when the tip has a deep subwavelength size, the tip is modeled by a superposition of electric and magnetic dipoles with moments $\mathbf{p}$ and $\mathbf{m}$, respectively, and the time-averaged photoinduced force exerted on the tip is[40] $\langle \mathbf{F} \rangle_t = \frac{1}{2}\mathrm{Re}[(\nabla \mathbf{E}^{\mathrm{loc}})^* + \mathbf{p}\cdot(\nabla \mathbf{H}^{\mathrm{loc}})^* \cdot \mathbf{m} - \frac{ck^4}{6\pi}(\mathbf{p} \times \mathbf{m}^*)]$ in which the local fields are considered at the position of the tip, ∇ denotes the gradient of the corresponding vector field, c is the speed of light in a vacuum, and k is the illumination wavenumber. In the following we neglect the magnetic dipole induced on the tip, since in a plasmonic tip the electric dipolar response will be dominant. The electric dipole generated on the tip is related to the local exciting field by $\mathbf{p} = \underline{\boldsymbol{\alpha}}_{\mathrm{tip}} \cdot \mathbf{E}^{\mathrm{loc}}$, where $\underline{\boldsymbol{\alpha}}_{\mathrm{tip}}$ is the electric polarizability tensor of the tip.

Under external illumination, the very end of the tip, which resembles a nano*grain*, is polarized as an electric dipole. The

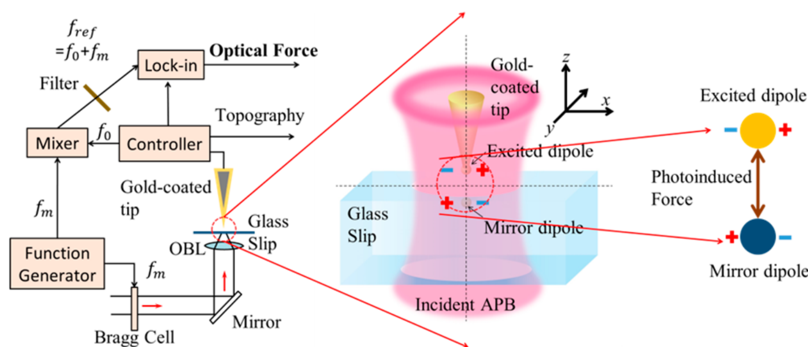

Figure 3. (Left) Schematic of the PiFM system established to characterize the sharply focused APB. (Right) Schematic of the dipole-like excitation of the gold-coated tip under sharply focused APB illumination and its interaction with the image in the substrate.

DOI: 10.1021/acsphotonics.7b00816
ACS Photonics 2018, 5, 390−397

PiFM probe tip is coated with a thin layer of gold to enhance its electric scattering response. As shown in refs 17, 32, 41, and 42, when the tip is close to a substrate surface, a mirror-image is created in the substrate that interacts with the tip. This tip−substrate system exposed to an electromagnetic field can be modeled by two interacting dipoles, namely, the tip dipole and its image dipole generated in the substrate, with polarizability $\boldsymbol{\alpha}_{\text{img}}$. Hence, the photoinduced force in the PiFM system is dominated by the photoinduced dipole−dipole interaction force, indicated in Figure 3 (right). That is, the influence of the gradient of the illumination beam and also the interaction due to higher order multipoles between the tip and image are neglected. Although this dipole−dipole force can contain both longitudinal and transverse components, only longitudinal force is acquired in our specific PiFM system, which operates in the ac tapping mode in the longitudinal direction. Hence the measured photoinduced force is the longitudinal dipole−dipole interaction force, which contains the contributions from both the transverse and longitudinal electric fields, and in the case of a tip with azimuthal symmetry (i.e., $\alpha_{\text{tip,t}} = \alpha_{\text{tip},x} = \alpha_{\text{tip},y}$) the force is given by (see Supporting Information)

$$\langle F \rangle_{\text{t}} \propto \frac{1}{d^4}\text{Re}[(\alpha_{\text{tip,t}}E_{\text{t}})(\alpha_{\text{img,t}}E_{\text{t}})^* - 2(\alpha_{\text{tip},z}E_z)(\alpha_{\text{img},z}E_z)^*] \tag{4}$$

Here $\alpha_{\text{tip,t}}$, $\alpha_{\text{img,t}}$, $\alpha_{\text{tip},z}$, and $\alpha_{\text{img},z}$ represent the polarizability of the tip and mirror-image dipole along the transverse and longitudinal directions, respectively, d represents the distance between the tip dipole and the image dipole, and E_{t} and E_z represent the transverse and longitudinal components of the incident electric field at the position of the tip, respectively. Note that eq 4 can directly be obtained from the Lorentz force or equivalently from the Maxwell stress tensor analysis, if one considers only the contribution of electric dipoles and neglects the contributions of all higher order multipoles (including magnetic dipoles, electric/magnetic quadrupoles, etc.). This is justified since the tip and its image are small compared to the wavelength. Moreover, in the calculation of eq 4, the phase difference of the incident beam between the tip and its image (i.e., quasi-static approximation) is neglected due to their deep-subwavelength distance. This expression can be further simplified for this particular case: first, since the APB ideally has no longitudinal electric field component regardless of focusing,[4,15] we only consider the transverse field contribution to the photoinduced force. Then, the polarizability of the image dipole is proportional to the tip dipole, i.e., $\alpha_{\text{tip,t}} \propto \alpha_{\text{img,t}}$. Lastly, in ac tapping mode, the distance between the two dipoles is constant in our PiFM operation, so we exclude the distance part from the expression. In summary, the photoinduced force is proportional to

$$\langle F \rangle_{\text{t}} \propto |\alpha_{\text{tip,t}}E_{\text{t}}|^2 \tag{5}$$

This expression indicates that the photoinduced force measured by the PiFM is proportional to the square of the product between the transverse tip polarizability and the incident transverse electrical field of the APB. Depending on the realistic geometry of the PiFM fabricated tip-end, its polarizability often shows a degree of azimuthal anisotropy. This anisotropy of the tip polarizability will have a substantial impact on the PiFM measurement as discussed later on in this paper.

MULTIFREQUENCY METHOD TO EXTRACT PHOTOINDUCED FORCE SIGNAL

After understanding the origin of the photoinduced force, the next key step is to clarify the way the time-average photoinduced force is measured. This is realized by applying the multifrequency method and lock-in mechanism in the system. Shown in Figure 3 left, the incident APB light field is modulated by the Bragg cell with a frequency f_{m} and then focused on the PiFM tip, which is vibrating at the first mechanical oscillation frequency f_0 of the cantilever. As explained in the previous section, a mirror dipole of the tip dipole is induced in the glass slip as shown in Figure 3. Here, the total tip−slip interaction force contains both the components of photoinduced force and nonphotoinduced force. Alternating on and off the modulated incident beam, the photoinduced force will be present and absent accordingly, while the nonphotoinduced force, containing all chemical, Casimir, meniscus, atomic, and van der Waals forces between tip and slip that contribute to the AFM topography measurement, will remain constant. Meanwhile, a wave mixer mixes the two control signals with frequencies of f_0 and f_{m}, respectively, to produce the sidebands $f_0 + f_{\text{m}}$ and $f_0 - f_{\text{m}}$, from which the $f_0 + f_{\text{m}}$ component is selected by an optical filter as the lock-in reference f_{ref}. Finally, by the lock-in mechanism between the reference and the AFM readout, the signal of the photoinduced force is efficiently extracted. A particular value of f_{m} is chosen to make f_{ref} exactly at the second mechanical resonant oscillation frequency of the cantilever to exploit its high Q-factor to enhance the signal-to-noise ratio. Here, our PiFM system includes a commercial AFM Veeco Caliber with a gold-coated tip from AppNano, with f_0 = 65 kHz, coated by sputtering deposition with approximately 25 nm of gold and 2 nm of adhesive chromium layers in ac tapping mode. The SEM image of the gold-coated tip and the measured force map is shown in Figure 4.

RESULTS AND DISCUSSION

The measured force map of the APB near field in Figure 4 shows a donut-shaped profile with a subwavelength feature, which agrees well with a typical sharply focused APB. The clear visualization of the many small dots in the force map, which are induced by the defects in the glass coverslip, excellently demonstrates the nanoscale resolution in our system. The resolution accuracy of this measurement is dependent on the size of the gold grain exactly on the end of the tip,[33] usually close to a few nanometers. In principle, the size of the deposited gold grain at the tip-end can be controlled by the sputtering deposition process, and smaller grains on the tip could also be achieved. However, as the grain becomes smaller, the photoinduced force is also weakened, thus decreasing the signal-to-noise ratio. Eventually, we optimize our deposition technique to make the best balance between resolution and signal-to-noise ratio.

There are three differences between the measured force map and the expected APB field that need careful considerations. First, a background noise can be observed which makes a nonzero force even far away from the beam. This noise is due to the thermally induced cantilever oscillation, which is constantly distributed in the measurement area.[17,29] More importantly at the APB center of the force map, the force amplitude is noticeably larger than the background. Finally the force profile of the APB in Figure 4 exhibits an asymmetric

DOI: 10.1021/acsphotonics.7b00816
ACS Photonics 2018, 5, 390−397

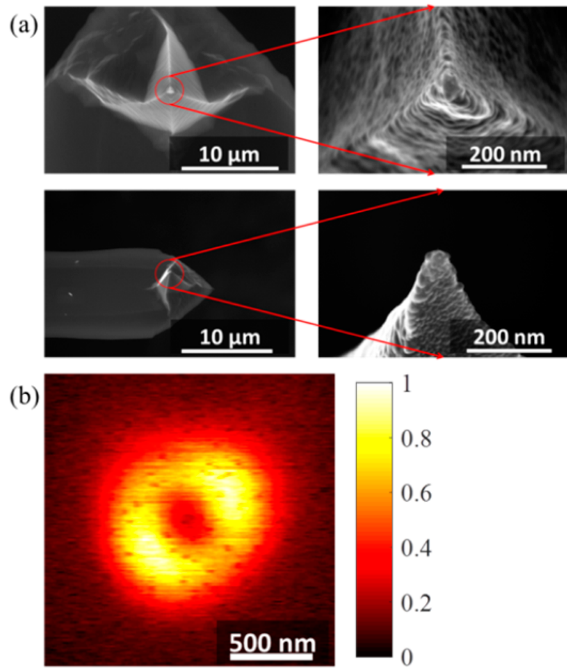

Figure 4. (a) SEM images of the gold-coated tip, with a top view (top panels), and with a 25° tilted view (bottom panels). (b) PiFM direct force measurement of the near field of the APB.

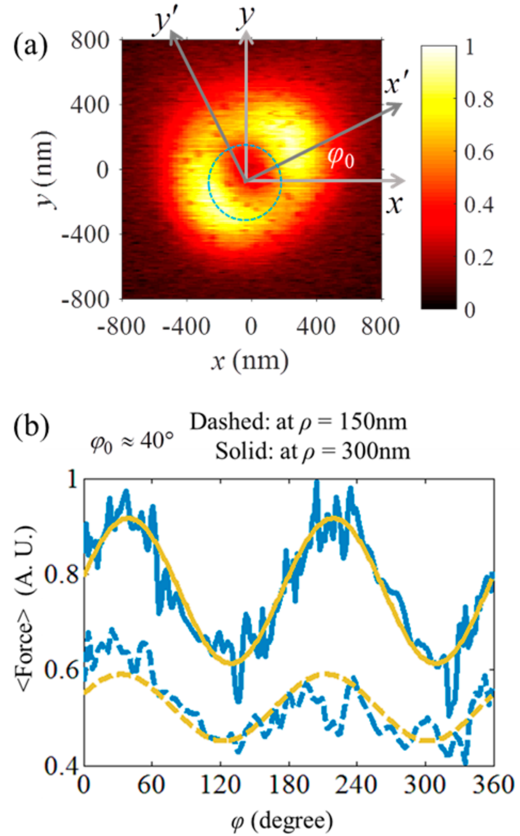

Figure 5. (a) Anisotropy axes in the measured PiFM force map (normalized to its maximum). (b) Force versus azimuthal angle at two different radial distances from the beam axis. Measured data (blue curves) are fit with the azimuthal-variation curves (yellow curve) from eq 8.

donut profile with obvious maximum and minimum amplitude on orthogonal axes. The last aspect should be attributed to the PiFM measurement rather than the incident APB, because as shown from the CCD image in Figure 2, the APB exhibits a rather good symmetric and pure polarization distribution before focusing and felt by the PiFM tip. The physical origin of these measurement deviances is attributed to the fabricated tip-end in the PiFM, which has a non-negligible size compared to the beam features and has an irregular, i.e., asymmetric, tip shape as shown in Figure 4. As a result, the PiFM is not able to sense the zero field intensity at the APB center; instead it senses the overall field in the approximate area of the tip-end. Furthermore, because of its shape, the transverse polarizability of the tip is not azimuthally isotropic, causing an anisotropic force-field response. Considering these effects, we develop a theoretical modeling to correct the measurement-induced anisotropy and retrieve the true intensity profile of the APB. To start, we model the overall tip as a polarizable scatterer with anisotropic polarizability:

$$\underline{\boldsymbol{\alpha}}_{\mathrm{tip}} = \alpha_{x'}\hat{\mathbf{x}}'\hat{\mathbf{x}}' + \alpha_{y'}\hat{\mathbf{y}}'\hat{\mathbf{y}}' \tag{6}$$

where the primed coordinates denote the anisotropy axes, rotated with respect to the nonprimed coordinate system shown in Figure 5. The anisotropy rotation angle between the primed and nonprimed coordinate axes is φ_0, so $\hat{\mathbf{x}}' = \cos\varphi_0\hat{\mathbf{x}} + \sin\varphi_0\hat{\mathbf{y}}$ and $\hat{\mathbf{y}}' = -\sin\varphi_0\hat{\mathbf{x}} + \cos\varphi_0\hat{\mathbf{y}}$. The force expression (eq 5) is straightforwardly updated taking into account the transversely anisotropic polarizability of the AFM tip as (see eq A.8 in the Supporting Information, where we assume $\underline{\boldsymbol{\alpha}}_{\mathrm{img}} \propto \underline{\boldsymbol{\alpha}}_{\mathrm{tip}}$):

$$\langle F\rangle_{\mathrm{t}} \propto |\underline{\boldsymbol{\alpha}}_{\mathrm{tip}}\cdot\mathbf{E}|^2 \tag{7}$$

where the force is treated as solely due to transverse electric field. From eqs 6 and 7 and after some algebraic steps, considering a constant thermal noise in the AFM system that contributes to the background noise floor, the final measured force map and field relation can be expressed as

$$\langle F\rangle_{\mathrm{t}} \propto |E^{\mathrm{APB}}(\rho)|^2\left[1 - \frac{B}{A}\cos[2(\varphi - \varphi_0)]\right] + I_{\mathrm{n}} \tag{8}$$

where $A = \frac{1}{2}(|\alpha_{x'}|^2 + |\alpha_{y'}|^2)$and $B = \frac{1}{2}(|\alpha_{x'}|^2 - |\alpha_{y'}|^2)$, and I_{n} represents background noise uniformly distributed in the force map.

According to eq 8, the photoinduced force distribution of the APB at constant radius ρ has a sinusoidal dependence on the azimuthal position. This analytical azimuthal variation is used to fit the experimental measured force map at two different radial distances from the beam axis, e.g., at ρ = 150 nm and ρ = 300 nm, exhibiting a very good match as shown in Figure 5(b). This result also confirms our assumption in eq 8 that the tip acts as the polarizable scatterer with azimuthal anisotropy. Note that the small darker spots scattered in the donut-shaped force map correspond to the sharp spikes in Figure 5(b). The fitted model filters out these spikes and at the same time describes the anisotropic tip polarizability.

On the basis of the fitted modeling, we can eliminate the trigonometrically oscillating term by averaging the force over the azimuthal angle φ, leading to

$$\langle F\rangle_{\mathrm{t},\varphi} \propto |E_{\varphi}(\rho)|^2 + I_{\mathrm{n}} \tag{9}$$

where $\langle F\rangle_{\mathrm{t},\varphi}$ denotes both the time and azimuthal averages of the photoinduced force, and based on the APB model in eq 1,

DOI: 10.1021/acsphotonics.7b00816
ACS Photonics 2018, 5, 390−397

the electric field intensity at the minimum-waist plane (i.e., $z = 0$) is given by

$$|E_{\varphi}(\rho)|^2 = \left| \frac{V}{\sqrt{\pi}} \frac{2\rho}{w_0{}^2} \mathrm{e}^{-(\rho/w_0)^2} \right|^2 \tag{10}$$

Next we numerically fit the radial dependence of the experimental force data with the APB radial variation in eq 9 using the parameters V, w_0, and I_n as shown in Figure 6(a). In doing so, we assume that the electric field intensity profile is the same as the force profile as implied by eq 9.

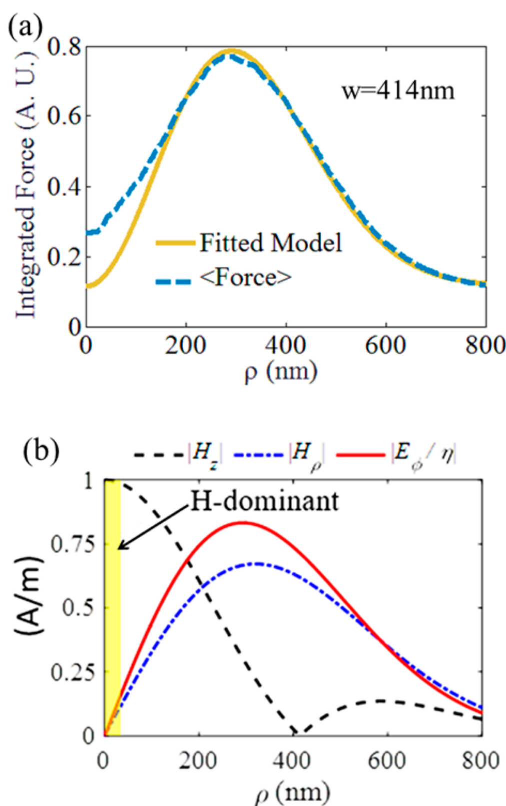

Figure 6. (a) Experimental result of azimuthal-average force versus radial distance ρ from the beam axis and fitting model in eq 9. (b) Inferred azimuthal electric field and the longitudinal magnetic field based on eq 1 and eq 11. The yellow highlight shows the region such that the local field admittance $F_Y = \eta|H_z/E_\rho| > 10$.

On the basis of the fitting process to match the experiment data we estimate that the beam parameter is $w_0 = 414$ nm, while the parameter V in the field formula given in eq 1 with eq 2 serves as a scaling coefficient for the beam strength. The fitting noise value is estimated as $I_n \approx (|V|/w_0)^2/25$. The SNR, defined as the peak intensity in the APB divided by the fitted background noise, is about 8 in this measurement. Our measured force map clearly exhibits the donut shape of the APB with clearly distinguishable boundaries and center darkness, in contrast to other reported field maps of similar structured light acquired by NSOM in previous works.[13,28−30] Further, the overall measurement and processing in PiFM here do not need any additional delicate interferometry-based cleaning mechanism as illustrated in ref 13, which gives PiFM a great advantage in measurement convenience and stability compared to the NSOM technique. It is noteworthy that the AFM used here in the PiFM system is a relatively old model. The field characterization performance is expected to be greatly improved if using the most state-of-the-art PiFM system, e.g., the Vistascope from Molecular Vista,[43] which has almost one-third the thermal noise as the Veeco Caliber system used here. Especially, the background noise in the force measurement can be greatly suppressed in a low-temperature vacuum environment, while NSOM can not benefit from it. Lastly, we recall that the power of the incident laser beam to the PiFM system is relatively low at 90 μW, which is limited by the maximum power of our laser diode. It is possible to significantly increase the SNR by using a much more powerful laser source. These improvements should be able to easily further increase the SNR on sharply focused structured light to about 40:1.

The fitted curve in Figure 6 represents the radial variation of the azimuthally averaged force very well except for some discrepancy occurring for a small radius because of the non-negligible size of the PiFM tip-end. Indeed, the tip-end size is not able to sample the electric field when vanishing at the center of the beam as explained before. The CFWHM and the electric field peak's location of the APB are calculated according to eq 3 as 282 and 289 nm, respectively. The corresponding magnetic field associated with the measured APB's electric field distribution is then calculated by using Maxwell's equation $\mathbf{H} = \nabla \times \mathbf{E}/(\mathrm{i}\omega\mu)$ and plotted in Figure 6(b). Assuming that the probe is at the minimum waist of the APB (i.e., $z = 0$), the longitudinal and radial magnetic field components are calculated as

$$\begin{aligned} H_z &= -\frac{V}{\eta} \frac{2\mathrm{i}}{\sqrt{\pi^3}} \frac{\lambda}{w_0{}^2} \mathrm{e}^{-(\rho/w_0)^2} \left(1 - \frac{\rho^2}{w_0{}^2}\right) \\ H_\rho &= -\frac{1}{\eta} E_\varphi \left[1 + \frac{1}{kz_R} \frac{\rho^2 - 2w_0{}^2}{w_0{}^2}\right] \end{aligned} \tag{11}$$

The magnetic dominant region, where the local field admittance $F_Y = \eta|H_z/E_\rho|$ is 10 times that of a plane wave, is confined in a region around the APB axis with a radius of 22 nm, as shown in yellow highlighting in Figure 6(b).

Next we finally report the force map of the raw and processed measurements. The measured force intensity, the fitted APB intensity from eq 9 with the background noise term I_n, and the fitted APB intensity only, with background noise removed, are reported in Figure 7 from left to right, respectively. Compared to the original force map of a sharply focused APB in Figure 7, left, the retrieval procedure that eliminates the anisotropy due to the probe tip restores the symmetric profile in both shape and amplitude. Furthermore, as explained above, the correction mechanism is able to calculate

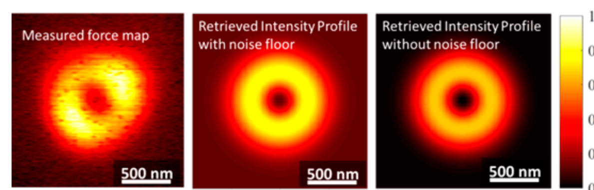

Figure 7. (Left) Measured force map of the sharply focused APB directly obtained by PiFM. (Middle) Corrected intensity distribution of the sharply focused APB obtained by using the fitted model with a noise floor. (Right) Same as in the middle panel with the difference that the background noise has been removed.

DOI: 10.1021/acsphotonics.7b00816
ACS Photonics 2018, 5, 390−397

and remove the background noise, and the final appearance of the sharply focused APB is revealed in Figure 7, right.

■ CONCLUSION

We have discussed some critical principles of the PiFM direct characterization of the intensity distribution of the sharply focused APB by directly performing near-field gradient force measurements with nanoscale accuracy. The measured force map shows excellent details of the subwavelength donut-shaped feature of the APB, although it exhibits a certain degree of asymmetry induced by the Au-coated probe tip-end. Then, we have fit the experimental data and corrected the measured asymmetry. Finally, on the basis of the fitted model, we calculate the corresponding APB parameters to reveal the final dimension of the beam such as its complementary full width at half-maximum as well as its magnetic field distribution, showing a magnetic dominant region near the APB axis. The magnetic dominant region of the APB is a promising feature for a plethora of optical magnetic applications. Indeed, we expect the APB to have a fundamental importance in future microscopy or near-field systems that involve detection and use of photo-induced magnetism.

This work also demonstrates the capability of the PiFM to reliably characterize sharply focused structured light in general, directly in the near field, which is an important tool to further explore light−matter interactions. The interpretation of the field distribution from the measured force map is significantly dependent on the realistic polarizability of the microscope tip-end. Hence, it is important to note that the APB can serve as a standard incident beam to calibrate the transverse polarizability of a microscope tip-end following the steps outlined in this paper.

■ ASSOCIATED CONTENT

Supporting Information

The Supporting Information is available free of charge on the ACS Publications website at DOI: 10.1021/acsphotonics.7b00816.

The derivation process of the photoinduced force exerted on the tip from the sharply focused APB, i.e., eq 4 and eq 7 (PDF)

■ AUTHOR INFORMATION

Corresponding Authors

*E-mail: hkwick@uci.edu.
*E-mail: f.capolino@uci.edu.

ORCID

Jinwei Zeng: 0000-0001-5795-2406

Author Contributions

F.C. and H.K.W. conceived the ideas of this work; J.Z. and F.H. performed the customary tip fabrication and characterization experiment; C.G., M.V., and M.A. developed the theoretical model for analysis and evaluation of experimental results. The manuscript was written through contributions of all authors. All authors have given approval to the final version of the manuscript.

Notes

The authors declare no competing financial interest.

■ ACKNOWLEDGMENTS

This work was supported by the W. M. Keck Foundation (USA) and the NSF Center for Chemical Innovation - Chemistry at the Space-Time Limit (CHE-1414466).

■ REFERENCES

(1) Guclu, C.; Tamma, V. A.; Wickramasinghe, H. K.; Capolino, F. Photoinduced magnetic force between nanostructures. *Phys. Rev. B: Condens. Matter Mater. Phys.* **2012**, *92*, 235111.
(2) Veysi, M.; Guclu, C.; Capolino, F. Vortex beams with strong longitudinally polarized magnetic field and their generation by using metasurfaces. *J. Opt. Soc. Am. B* **2015**, *32*, 345−54.
(3) Veysi, M.; Guclu, C.; Capolino, F. Large magnetic to electric field contrast in azimuthally polarized vortex beams generated by a metasurface. *Proc. SPIE* **2015**, *9544*, 954408.
(4) Zhan, Q. Cylindrical vector beams: from mathematical concepts to applications. *Adv. Opt. Photonics* **2009**, *1*, 1.
(5) Guclu, C.; Veysi, M.; Capolino, F. Photoinduced Magnetic Nanoprobe Excited by an Azimuthally Polarized Vector Beam. *ACS Photonics* **2016**, *3*, 2049−58.
(6) Youngworth, K. S.; Brown, T. G. Focusing of high numerical aperture cylindrical-vector beams. *Opt. Express* **2000**, *7*, 77−87.
(7) Kasperczyk, M.; Person, S.; Ananias, D.; Carlos, L. D.; Novotny, L. Excitation of magnetic dipole transitions at optical frequencies. *Phys. Rev. Lett.* **2015**, *114*, 163903.
(8) Veysi, M.; Guclu, C.; Capolino, F. Focused azimuthally polarized vector beam and spatial magnetic resolution below the diffraction limit. *J. Opt. Soc. Am. B* **2016**, *33*, 2265−77.
(9) Karaveli, S.; Zia, R. Optical Frequency Magnetic Dipole Transitions. In *Encyclopedia of Nanotechnology*; Springer: The Netherlands, 2012; pp 1942−50.
(10) Noginova, N.; Zhu, G.; Mavy, M.; Noginov, M. Magnetic dipole based systems for probing optical magnetism. *J. Appl. Phys.* **2008**, *103*, 07E901.
(11) Burresi, M.; Van-Oosten, D.; Kampfrath, T.; Schoenmaker, H.; Heideman, R.; Leinse, A.; Kuipers, L. Probing the magnetic field of light at optical frequencies. *Science* **2009**, *326*, 550−3.
(12) Zhan, Q. Trapping nanoparticles with cylindrical polarization. *In Proc. SPIE*, the SPIE 49th Annual Meeting 2004; pp 275−28210.1117/12.558780.
(13) Bauer, T.; Orlov, S.; Peschel, U.; Banzer, P.; Leuchs, G. Nanointerferometric amplitude and phase reconstruction of tightly focused vector beams. *Nat. Photonics* **2014**, *8*, 23−7.
(14) Neugebauer, M.; Woźniak, P.; Bag, A.; Leuchs, G.; Banzer, P. Polarization-controlled directional scattering for nanoscopic position sensing. *Nat. Commun.* **2016**, *7*, 11286.
(15) Chen, Z.; Hua, L.; Pu, J. Tight focusing of light beams: effect of polarization, phase and coherence. *Prog. Opt.* **2012**, *57*, 219−59.
(16) Martin, Y. C.; Hamann, H. F.; Wickramasinghe, H. K. Strength of the electric field in apertureless near-field optical microscopy. *J. Appl. Phys.* **2001**, *89*, 5774−8.
(17) Huang, F.; Tamma, V. A.; Mardy, Z.; Burdett, J.; Wickramasinghe, H. K. Imaging nanoscale electromagnetic near-field distributions using optical forces. *Sci. Rep.* **2015**, *5*, 10610.
(18) Betzig, E.; Trautman, J.; Harris, T.; Weiner, J.; Kostelak, R. Breaking the diffraction barrier-optical microscopy on a nanometric scale. *Science* **1991**, *251*, 1468−70.
(19) Fleischer, M.; Stanciu, C.; Stade, F.; Stadler, J.; Braun, K.; Heeren, A.; Häffner, M.; Kern, D. P.; Meixner, A. J. Three-dimensional optical antennas: Nanocones in an apertureless scanning near-field microscope. *Appl. Phys. Lett.* **2008**, *93*, 111114.
(20) Le-Feber, B.; Rotenberg, N.; Beggs, D.; Kuipers, L. Simultaneous measurement of nanoscale electric and magnetic optical fields. *Nat. Photonics* **2014**, *8*, 43−6.
(21) García-Etxarri, A.; Romero, I.; Garcia de-Abajo, F. J.; Hillenbrand, R.; Aizpurua, J. Influence of the tip in near-field imaging of nanoparticle plasmonic modes: Weak and strong coupling regimes. *Phys. Rev. B: Condens. Matter Mater. Phys.* **2009**, *79*, 125439.

DOI: 10.1021/acsphotonics.7b00816
ACS Photonics 2018, 5, 390−397

(22) Esslinger, M.; Vogelgesang, R. Reciprocity theory of apertureless scanning near-field optical microscopy with point-dipole probes. *ACS Nano* **2012**, *6*, 8173−82.
(23) Hecht, B.; Sick, B.; Wild, U. P.; Deckert, V.; Zenobi, R.; Martin, O. J.; Pohl, D. W. Scanning near-field optical microscopy with aperture probes: Fundamentals and applications. *J. Chem. Phys.* **2000**, *112*, 7761−74.
(24) Nowak, D.; Morrison, W.; Wickramasinghe, H. K.; Jahng, J.; Potma, E. O.; Wan, L.; Ruiz, R.; Albrecht, T. R.; Schmidt, K.; Frommer, J.; Sanders, D. P. Nanoscale chemical imaging by photoinduced force microscopy. *Sci. Adv.* **2016**, *2*, e1501571.
(25) Schmid, T.; Opilik, L.; Blum, C.; Zenobi, R. Nanoscale chemical imaging using tip-enhanced Raman spectroscopy: a critical review. *Angew. Chem., Int. Ed.* **2013**, *52*, 5940−54.
(26) Ocelic, N.; Huber, A.; Hillenbrand, R. Pseudoheterodyne detection for background-free near-field spectroscopy. *Appl. Phys. Lett.* **2006**, *89*, 101124.
(27) Zenhausern, F.; Martin, Y.; Wickramasinghe, H. K. Scanning interferometric apertureless microscopy: optical imaging at 10 angstrom resolution. *Science* **1995**, *269*, 1083.
(28) Debus, C.; Lieb, M. A.; Drechsler, A.; Meixner, A. J. Probing highly confined optical fields in the focal region of a high NA parabolic mirror with subwavelength spatial resolution. *J. Microsc.* **2003**, *210*, 203−208.
(29) Zhang, M.; Wang, J. Plasmonic lens focused longitudinal field excitation for tip-enhanced Raman spectroscopy. *Nanoscale Res. Lett.* **2015**, *10*, 189.
(30) Lerman, G. M.; Yanai, A.; Levy, U. Demonstration of Nanofocusing by the use of Plasmonic Lens Illuminated with Radially Polarized Light. *Nano Lett.* **2009**, *9*, 2139−43.
(31) Kohoutek, J.; Dey, D.; Bonakdar, A.; Gelfand, R.; Sklar, A.; Memis, O. G.; Mohseni, H. Opto-mechanical force mapping of deep subwavelength plasmonic modes. *Nano Lett.* **2011**, *11*, 3378−82.
(32) Jahng, J.; Brocious, J.; Fishman, D. A.; Huang, F.; Li, X.; Tamma, V. A.; Wickramasinghe, H. K.; Potma, E. O. Gradient and scattering forces in photoinduced force microscopy. *Phys. Rev. B: Condens. Matter Mater. Phys.* **2014**, *90*, 155417.
(33) Jahng, J.; Brocious, J.; Fishman, D. A.; Yampolsky, S.; Nowak, D.; Huang, F.; Apkarian, V. A.; Wickramasinghe, H. K.; Potma, E. O. Ultrafast pump-probe force microscopy with nanoscale resolution. *Appl. Phys. Lett.* **2015**, *106*, 083113.
(34) Rajapaksa, I.; Uenal, K.; Wickramasinghe, H. K. Image force microscopy of molecular resonance: A microscope principle. *Appl. Phys. Lett.* **2010**, *97*, 073121.
(35) Tumkur, T. U.; Yang, X.; Cerjan, B.; Halas, N. J.; Nordlander, P.; Thomann, I. Photoinduced Force Mapping of Plasmonic Nanostructures. *Nano Lett.* **2016**, *16*, 7942−9.
(36) Stalder, M.; Schadt, M. Linearly polarized light with axial symmetry generated by liquid-crystal polarization converters. *Opt. Lett.* **1996**, *21*, 1948−50.
(37) Garcia, R.; Herruzo, E. T. The emergence of multifrequency force microscopy. *Nat. Nanotechnol.* **2012**, *7*, 217−26.
(38) Nieto-Vesperinas, M.; Sáenz, J.; Gómez-Medina, R.; Chantada, L. Optical forces on small magnetodielectric particles. *Opt. Express* **2010**, *18*, 11428−43.
(39) Jackson, J. D. In *Classical Electrodynamics*; John Wiley & Sons, 1999; pp 237−294 and 407−455.
(40) Chaumet, P. C.; Rahmani, F. Electromagnetic force and torque on magnetic and negative-index scatterers. *Opt. Express* **2009**, *17*, 2224−2234.
(41) Chaumet, P. C.; Nieto-Vesperinas, M. Coupled dipole method determination of the electromagnetic force on a particle over a flat dielectric substrate. *Phys. Rev. B: Condens. Matter Mater. Phys.* **2000**, *61*, 14119.
(42) Wang, S. B.; Chan, C. T. Lateral optical force on chiral particles near a surface. *Nat. Commun.* **2014**, *5*, 3307.
(43) http://molecularvista.com/product/vistascope/.

DOI: 10.1021/acsphotonics.7b00816
ACS Photonics 2018, 5, 390−397